

Late-time X-ray afterglows of GRBs: Implications for particle acceleration at relativistic shocks

Zhi-Qiu Huang,¹ Om Sharan Salafia,^{2,3} Lara Nava,^{2,4} Annalisa Celotti,^{1,2,4,5} and Giancarlo Ghirlanda²

¹ SISSA, Via Bonomea 265, I-34136 Trieste, Italy

² INAF - Osservatorio Astronomico di Brera, Via E. Bianchi, 46, I-23807 Merate, Italy

³ INFN - Sezione di Milano-Bicocca, Piazza della Scienza 3, I-20126 Milano, Italy

⁴ INFN - Sezione di Trieste, Via Valerio 2, I-34127 Trieste, Italy

⁵ IFPU - Institute for Fundamental Physics of the Universe, Via Beirut 2, I-34151 Trieste, Italy

Accepted XXX. Received YYY; in original form ZZZ

ABSTRACT

Particle-in-cell (PIC) numerical simulations are currently among the most advanced tools to investigate particle acceleration at relativistic shocks. Still, they come with limitations imposed by finite computing power, whose impact is not straightforward to evaluate a priori. Observational features are hence required as verification. Gamma-ray burst (GRB) afterglow emission, produced by high-energy electrons accelerated at external shocks, provides a testbed for such predictions. Current numerical studies suggest that in GRB afterglows the maximum synchrotron photon energy, which corresponds to the limit of electron acceleration, may fall within the $\sim 0.1\text{--}10$ keV X-ray energy band at late times, $t \gtrsim 10^6\text{--}10^7$ s. To test this prediction, we analyzed the X-ray spectra of six GRBs with *Swift*/XRT detections beyond 10^7 s: our analysis reveals no clear evidence of a spectral cutoff. Using a model that accounts for the effect of the finite opening angle of the shock on the observed maximum synchrotron photon energy, we show that these observations are incompatible with PIC simulation predictions, unless one or more physical afterglow parameters attain values at odds with those typically inferred from afterglow modeling (small radiative efficiency, low ambient density, large equipartition fraction ϵ_B of the magnetic field). These findings challenge existing numerical simulation results and imply a more efficient acceleration of electrons to high-energies than seen in PIC simulations, with important implications for our understanding of particle acceleration in relativistic shocks.

Key words. Radiation mechanisms: non-thermal - Gamma ray bursts - Acceleration of particles

1. Introduction

The emission properties of gamma-ray bursts (GRBs) have been extensively studied through numerous observations. According to the standard model, an 'external' relativistic shock forms and propagates outward through the surrounding medium. As the shock propagates, it interacts with the ambient material and accelerates electrons to very high energies (Meszaros et al. 1994; Dermer & Chiang 1998). These accelerated particles produce a long-lasting afterglow emission through both the synchrotron and the synchrotron self-Compton (SSC) processes (Sari et al. 1998; Chiang & Dermer 1999; Sari & Esin 2001), with detectable emission persisting in some cases for several months after the burst.

Numerical simulations suggest that weakly-magnetized relativistic shocks - characteristic of GRB afterglows - are mediated by the Weibel instability (Weibel 1959; Medvedev & Loeb 1999; Spitkovsky 2005, 2008; Sironi & Spitkovsky 2009b; Sironi et al. 2013). Particles undergo repeated scattering by small-scale turbulence generated through the instability, allowing them to cross the shock front multiple times and gain energy. The afterglow radiation produced by these accelerated electrons encodes detailed information about particle acceleration at relativistic shocks.

The maximum synchrotron photon energy, directly related to the maximum accelerated electron energy, is crucial to study the detailed acceleration process as well as the microphysical conditions of the environment near the shock. An often invoked limit

for the maximum energy (e.g., Piran & Nakar 2010; Ackermann et al. 2014; Pennanen et al. 2014) is the so-called synchrotron burnoff limit, where the synchrotron cooling rate is balanced by the idealized fastest Bohm-diffusion acceleration rate (de Jager et al. 1996; Dermer & Menon 2009), which can hardly occur. In numerical simulations by Sironi et al. (2013), where more realistic acceleration processes are considered, the acceleration rate is found to be slower and the predicted maximum energy smaller than in the synchrotron burnoff limit case.

Starting from the result of Sironi et al. (2013), the maximum synchrotron photon energy emitted by accelerated electrons could potentially move into the energy band of the X-Ray Telescope (XRT, 0.3-10 keV) onboard the Niel Gehrels *Swift* Observatory during the late-time phase (10^6 - 10^7 s after the burst), producing observable features in the X-ray spectra. Until June 11th, 2025, the *Swift* XRT catalog contains 1745 GRBs¹ (Evans et al. 2007, 2009, 2023). We selected six events with XRT detections later than 10^7 s as well as measured redshifts, and analyzed their late-time X-ray spectra. By comparing the theoretical predictions with the results of our spectral analysis, implications can be obtained on shock acceleration.

This paper is organized as follows. In section 2 we summarize the predictions of Sironi et al. (2013) on the expected energy of synchrotron photons emitted by electrons reaching the acceleration limit during the late-time afterglow phase. We then refine

¹ https://swift.gsfc.nasa.gov/archive/grb_table/stats/

these predictions by taking into account that the observed radiation originates from an equal-arrival-time surface (EATS). The procedure and results of the data analysis of the selected GRB afterglows are described in section 3. The constraints on the GRBs physical parameters inferred from the comparison between the theoretical predictions and the observations are presented in section 4. In section 5 we discuss the results and draw our conclusions.

2. Maximum Synchrotron Photon Energy

2.1. Analytical prediction based on PIC simulations

In this section we recall the results by Sironi et al. (2013) on the maximum electron energies, under the assumption that the shock is ultra-relativistic.

When the cooling rate of electrons balances the acceleration rate (here only the energy losses due to synchrotron emission are considered), electrons can no longer gain energy and reach the cooling limit at a Lorentz factor γ_{syn} , corresponding to the typical synchrotron photon energy $h\nu_{\text{syn}}$. Adopting the acceleration rate estimated by Sironi et al. (2013), $h\nu_{\text{syn}}$ can be expressed as

$$h\nu_{\text{syn}} \simeq \begin{cases} 620 E_{k,54}^{1/4} n_0^{-1/12} \epsilon_{B,-3}^{-1/6} (1+z)^{-1/4} t_{\text{obs},7}^{-3/4} \text{ keV,} & \text{ISM} \\ 422 E_{k,54}^{1/3} A_{\star}^{-1/6} \epsilon_{B,-3}^{-1/6} (1+z)^{-1/3} t_{\text{obs},7}^{-2/3} \text{ keV,} & \text{wind} \end{cases} \quad (1)$$

where E_k is the isotropic shock kinetic energy, ϵ_B is the fraction of the shock energy that is carried by the downstream magnetic field, t_{obs} is the observer time and z is the redshift of the source. 'ISM' and 'wind' refer to the interstellar medium-like case (constant upstream number density $n = n_0$) and to the wind-like case ($n = A R^{-2}$, where R is the distance from the progenitor, and $A_{\star} = A/3 \times 10^{35} \text{ cm}^{-1}$ – Chevalier & Li 2000), respectively. We use the notation $Q_{\alpha} = Q/10^{\alpha}$ for all the quantities, in cgs units. The above estimate of $h\nu_{\text{syn}}$ neglects cooling induced by the synchrotron self-Compton (SSC) process, which is generally negligible at the times relevant to this study. This choice is conservative with respect to our conclusions.

Besides, the acceleration process quenches when the isotropization rate of downstream particles becomes smaller than their gyro-frequency, in which case downstream particles are constrained to move along the magnetic lines perpendicular to the shock normal and can hardly cross the shock. This happens when the particle energy reaches the so-called saturation, or magnetized, limit γ_{sat} , corresponding to a characteristic synchrotron photon energy (Sironi et al. 2013)

$$h\nu_{\text{sat}} \simeq \begin{cases} 2.85 E_{k,54}^{1/2} \epsilon_{B,-3}^{1/2} \sigma_{u,-9}^{-1/2} (1+z)^{1/2} t_{\text{obs},7}^{-3/2} \text{ keV,} & \text{ISM} \\ 2.10 E_{k,54}^{1/2} \epsilon_{B,-3}^{1/2} \sigma_{u,-9}^{-1/2} (1+z)^{1/2} t_{\text{obs},7}^{-3/2} \text{ keV,} & \text{wind} \end{cases} \quad (2)$$

where $\sigma_u = \frac{B_u^2}{4\pi m_p c^2}$ is the upstream magnetization parameter, B_u is the strength of the upstream magnetic field and m_p is the proton mass. In the wind case, we assume a toroidal magnetic field in the stellar wind that evolves as $B_u \propto R^{-1}$. Hence, σ_u is a constant.

In Fig. 1 we plot the maximum attainable photon energy $h\nu_{\text{max}} = \min[h\nu_{\text{syn}}, h\nu_{\text{sat}}]$ for different sets of afterglow parameters. A redshift $z = 0.2$ is adopted as a benchmark, since the redshifts of the six GRBs that we selected for the analysis lie between 0.07 and 0.35. For a typical range of values of the afterglow parameters, $h\nu_{\text{syn}}$ and $h\nu_{\text{sat}}$ intersect at t_{obs} much earlier

than 10^6 s, implying that for $t_{\text{obs}} \geq 10^6$ s, $h\nu_{\text{max}}$ is determined by $h\nu_{\text{sat}}$.

For GRBs with low energy and/or small ϵ_B , $h\nu_{\text{max}}$ falls within the 0.3 - 10 keV energy band (gray shaded area in Fig. 1) at about 10^6 s. This would result in an observational feature - a cutoff in the XRT spectra - that can be searched for in late time X-ray observational data.

2.2. Effects of emission from high latitudes

The predictions for the maximum synchrotron photon energy summarized in the previous section have been derived for emission from material moving along the line of sight. For an extended source expanding radially at relativistic speed, photons that are received by the observer at the same time actually originate at different latitudes and at different times. Due to the small radial width of the shock downstream, the region contributing the radiation observed at a fixed observer time approximately takes the form of a surface in space-time (the so-called equal-arrival-time surface – EATS, Panaiteescu & Mészáros 1998; Sari 1998; Huang et al. 2007), where radiation originated from higher latitudes is emitted earlier than that from lower latitudes. This surface approximation can be adopted since synchrotron photons with the maximum energy are produced by electrons concentrated near the shock front.

For a relativistic blast wave produced by a point explosion, the relation between the shock Lorentz factor Γ_{sh} and its radius R can be written as (Blandford & McKee 1976)

$$\Gamma_{\text{sh}}(R) = \left[\frac{(17-4k) E_k}{8\pi A m_p c^2 R^{3-k}} \right]^{1/2}, \quad (3)$$

where $k = 0$ for the ISM case or $k = 2$ for the wind case. The relation between the shock radius and the central engine frame time t is

$$R \approx c t / \left[1 + \frac{1}{2(4-k) \Gamma_{\text{sh}}^2} \right]. \quad (4)$$

Photons emitted at a time t by a portion of the shock located at a latitudinal angle θ (with respect to the line of sight) reach the observer at a time

$$t_{\text{obs}}/(1+z) = t - R \cos \theta / c. \quad (5)$$

Combining the above equations, one obtains an implicit equation that links the shock radius, the observer time and the latitude (Sari 1997), namely

$$R(\theta, t_{\text{obs}}) = \frac{c t_{\text{obs}} / (1+z)}{1 - \cos \theta + 1 / [2(4-k) \Gamma_{\text{sh}}^2(R)]}, \quad (6)$$

which can be solved numerically to determine the EATS, namely $R(\theta)$ for any fixed observer time.

We now illustrate how the observed radiation, and in particular the maximum observable synchrotron photon energy, is affected when the EATS is taken into account.

In the shock downstream comoving frame, the synchrotron power emitted by an electron is $P'_{\text{syn}}(\gamma_e) = \sigma_{\text{TC}} \gamma_e^2 B'^2 / 6\pi$ and the characteristic synchrotron frequency is $\nu'(\gamma_e) = \gamma_e^2 e B' / 2\pi m_e c$, where γ_e is the electron Lorentz factor, σ_{TC} is the Thomson cross section and m_e is the electron mass. B' is the strength of the comoving magnetic field, which can be expressed as $B' = (32\pi m_p c^2 \epsilon_B n)^{1/2} \Gamma$. The peak spectral power can be approximated as $P'_{\nu, \text{max}} \sim P'_{\text{syn}}(\gamma_e) / \nu'(\gamma_e) = \sigma_{\text{TC}} m_e c^2 B' / 3e$.

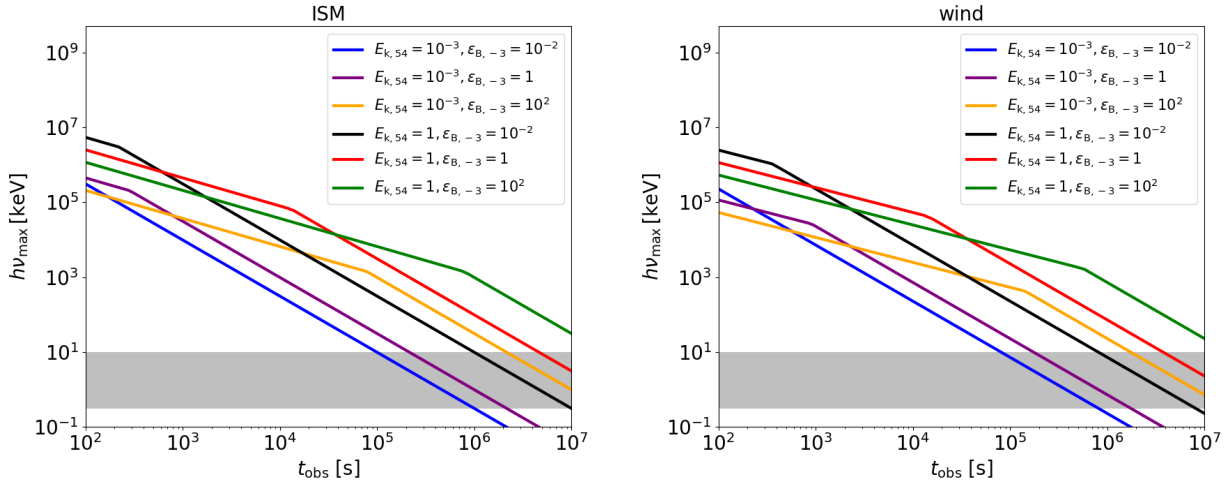


Fig. 1. Time evolution of the maximum synchrotron photon energy $h\nu_{\max} = \min [h\nu_{\text{syn}}, h\nu_{\text{sat}}]$ for different sets of afterglow parameters. The redshift is fixed at $z = 0.2$, and the upstream magnetization parameter is fixed to be $\sigma_u = 10^{-9}$. The gray shaded area indicates the energy band between 0.3 and 10 keV. Left panel: ISM case with $n_0 = 0.1$. Right panel: wind case with $A_{\star} = 1$. For $t_{\text{obs}} \geq 10^6$ s, $h\nu_{\max}$ is set by $h\nu_{\text{sat}}$ for all sets of parameters and can fall in the XRT energy band.

From optically thin radiative transfer, the radiation intensity at the shock, as measured in the downstream comoving frame, is $I'_{\nu'} = j'_{\nu'} \Delta'$, where Δ' is the effective width of the downstream region and $j'_{\nu'}$ is the synchrotron emissivity given by

$$j'_{\nu'}(\nu') = \frac{1}{4\pi} \int_{\gamma_{\min}}^{+\infty} \frac{dn'}{d\gamma_e}(\gamma_e) P'_{\nu',\text{syn}}(\gamma_e, \nu') d\gamma_e \quad (7)$$

$$\sim \frac{n' P'_{\nu',\max}}{4\pi} f(\nu').$$

Here $f(\nu')$ encodes the various power law regimes that arise from the above convolution of the single-particle synchrotron specific power $P'_{\nu',\text{syn}}$ with the electron energy distribution $dn'/d\gamma_e$. The latter is the result of electron acceleration at the shock and the consequent radiative (and eventually adiabatic) cooling as electrons are advected in the downstream region. For typical GRB afterglow parameters, and focusing on late times as those of our interest, this results (Sari et al. 1998; Sari & Esin 2001; Granot & Sari 2002) in a broken power law

$$\frac{dn'}{d\gamma_e} \propto \begin{cases} \gamma_e^{-p} & \gamma_{\min} < \gamma_e \leq \gamma_c, \\ \gamma_e^{-p-1} & \gamma_c < \gamma_e < \gamma_{\max}, \\ 0 & \text{otherwise,} \end{cases} \quad (8)$$

where p is the power law index of the injected electron distribution, which extends between γ_{\min} and γ_{\max} , and γ_c is the cooling Lorentz factor. Assuming $p > 2$ and $\gamma_{\max} \gg \gamma_{\min}$, we have

$$\gamma_{\min} \sim \epsilon_e \left(\frac{p-2}{p-1} \right) \frac{m_p}{m_e} \Gamma, \quad (9)$$

where ϵ_e is the fraction of the shock energy in relativistic electrons downstream and $\Gamma = \Gamma_{\text{sh}} / \sqrt{2}$ is the downstream Lorentz factor. The cooling Lorentz factor can be estimated as $\gamma_c m_e c^2 = P'_{\text{syn}}(\gamma_c) t'$, where $t' \simeq R/\Gamma c$.

For γ_{\max} we adopt the value estimated by Sironi et al. (2013), namely

$$\gamma_{\max} = \frac{2\Gamma m_p}{m_e \sigma_u^{1/4}}. \quad (10)$$

The resulting spectral shape can thus be expressed as

$$f(\nu') = \begin{cases} \left(\frac{\nu'}{\nu'_{\min}} \right)^{1/3} & \nu'_{\min} > \nu' \\ \left(\frac{\nu'}{\nu'_{\min}} \right)^{-(p-1)/2} & \nu'_c > \nu' > \nu'_{\min} \\ \left(\frac{\nu'_c}{\nu'_{\min}} \right)^{-(p-1)/2} \left(\frac{\nu'}{\nu'_c} \right)^{-p/2} e^{-\nu'/\nu'_{\max}} & \nu' > \nu'_c, \end{cases} \quad (11)$$

where ν'_{\min} , ν'_c and ν'_{\max} are the characteristic synchrotron frequencies of electrons with Lorentz factors γ_{\min} , γ_c and γ_{\max} , respectively. For simplicity we assume an exponential cutoff at $\nu' = \nu'_{\max}$ and neglect the synchrotron self-absorption, as it is not relevant at the frequencies of our interest.

Transforming to the observer frame, the radiation intensity is $I_{\nu}(\nu) = \mathcal{D}^3 I'_{\nu}(\nu/\mathcal{D}) = \mathcal{D}^3 j'_{\nu}(\nu/\mathcal{D}) \Delta'$, where $\mathcal{D} = [\Gamma(1 - \beta \cos \theta)]^{-1}$ is the relativistic Doppler factor.

Since the downstream comoving electron density $n' = N_e / 4\pi R^2 \Delta'$, where N_e is the number of electrons swept by an isotropic spherical shock, we have (see Eq. 7)

$$I_{\nu} = \mathcal{D}^3 \frac{N_e P'_{\nu,\max}}{16\pi^2 R^2} f(\nu/\mathcal{D}). \quad (12)$$

For a source located at a luminosity distance D_L , the total observed flux density is obtained by integrating over the equal-arrival-time surface (the solution to Eq. 6)

$$F_{\nu}(t_{\text{obs}}) \sim \frac{2\pi}{D_L^2} \int R^2(\theta, t_{\text{obs}}) I_{\nu}(\nu/\mathcal{D}, \theta, t_{\text{obs}}) \sin \theta d\theta, \quad (13)$$

which leads to

$$F_{\nu}(t_{\text{obs}}) = \frac{1}{2} \int \mathcal{D}^2 F_{\nu,\max} f(\nu/\mathcal{D}) \sin \theta d\theta, \quad (14)$$

where we defined $F_{\nu,\max} \equiv \mathcal{D} N_e P'_{\nu,\max} / 4\pi D_L^2$.

The relative contribution to the flux from different latitudes can be seen in Fig. 2 where we plot the differential flux $dF_{\nu}/d\theta$ at $\nu/\mathcal{D} > \nu'_c$ as a function of the latitudinal angles (at the time 3×10^6 s). Such contribution increases with the latitudinal angle

until it reaches a peak at a critical angle θ_c , where θ_c can be (numerically) estimated from

$$\theta_c = \sin^{-1} \left[\frac{1}{\Gamma(R(\theta, t_{\text{obs}}))} \right] \quad (15)$$

where $R(\theta, t_{\text{obs}})$ is given by Eq. 6.

The critical angle θ_c (marked with dotted vertical lines in Fig. 2) depends on the Lorentz factor of the shocked fluid. As time evolves, the shock decelerates and θ_c increases. In the case of a jet geometry - expected to be the most likely for GRB ejecta - θ_c is limited by the jet opening angle θ_j . The gray area in Fig. 2 represents a typical range for the jet opening angle, $\theta_j \in [0.05, 0.3]$ radians (Fong et al. 2012). At the late times considered in this work, θ_c can exceed θ_j . When this occurs, the flux is mainly contributed by the edge of the jet rather than by θ_c . This can be seen in Fig. 2: when $\theta_j < \theta_c$, most of the high-energy flux originates from the jet edge, while when $\theta_j \gtrsim \theta_c$, it arises predominantly from regions around θ_c .

In order to assess the effect of the jet opening angle on the observable $h\nu_{\text{max}}$ as a function of t_{obs} , we compare in Fig. 3 the values of $h\nu_{\text{max}}$ from Eq. 2, where the role of θ_j is neglected (blue solid line), with those obtained when the emission is produced at an angle $\min[\theta_c, \theta_j]$ (solid lines of other colors).

For the reason specified below, in the figure we show the latter one for different values of the jet break time t_j (as labeled), where

$$\begin{aligned} t_j &\sim (1+z) \theta_j^{8/3} \left[\frac{17 E_k}{512\pi n m_p c^5} \right]^{1/3} = \\ &= 1.4 \times 10^5 (1+z) \left(\frac{\theta_j}{0.1} \right)^{8/3} \left(\frac{E_{k,54}}{n_0} \right)^{1/3} \text{ s} \end{aligned} \quad (16)$$

for the ISM case (left panel), and

$$\begin{aligned} t_j &\sim (1+z) \theta_j^4 \left[\frac{9 E_k}{32\pi A m_p c^3} \right] = \\ &= 6.6 \times 10^5 (1+z) \left(\frac{\theta_j}{0.1} \right)^4 \left(\frac{E_{k,54}}{A_*} \right) \text{ s} \end{aligned} \quad (17)$$

for the wind case (right panel). For all values of t_j , the discrepancies between the two values of $h\nu_{\text{max}}$ are negligible when $\theta_c < \theta_j$, while when $\theta_c > \theta_j$ Eq. 2 overestimates the maximum photon energy since photons at $h\nu_{\text{max}}$ are mainly contributed from the edge of the jet. Note that the above expressions estimate t_j for ejecta along the line of sight. Since the radiation observed at energy $h\nu_{\text{max}}$ is mainly produced in high-latitudinal regions, the temporal breaks in the curves - which correspond to the time when $\theta_c = \theta_j$ - occur at (slightly) later times.

In Fig. 3 we also compare the expected values of $h\nu_{\text{max}}$ for parameters corresponding to the same jet break time t_j but different θ_j and $E_{k,54}$ (solid and dashed curves of the same color in the figure). While $h\nu_{\text{max}}$ are clearly different, their temporal dependence is not, being only determined by the jet break time t_j . Indeed, as analytically shown in Appendix B, the 'normalized' time evolution $h\nu_{\text{max}}(t_{\text{obs}})/h\nu_{\text{max}}(t_j)$ only depends on the time variable t_{obs}/t_j . As a result, the evolution of $h\nu_{\text{max}}$ is fully specified by the normalization of Eq. 2, which is proportional to the square root of $E_k \epsilon_B n_0 / B_u^2$ in the ISM case (and of $E_k \epsilon_B / \sigma_u$ in the wind case), and by the normalized time variable t_{obs}/t_j .

Viceversa, for a given observed $h\nu_{\text{max}}$ at a given time t_{obs} , it is possible to set constraints on the physical parameters. More precisely, for what just illustrated, such constraints can be meaningfully posed in the parameter space reported in Fig. 4, namely

$E_k \epsilon_B n_0 / B_u^2$ ($E_k \epsilon_B / \sigma_u$) in the ISM (wind) case vs the predicted t_j . The figure shows the resulting limits on these two quantities, assuming that photons with energy $h\nu_{\text{max}} = 3$ keV are emitted at the angle $\min[\theta_j, \theta_c]$ and observed at different times (as labeled). Note that here and in the following, instead of using σ_u we explicitly specify the values of the density and upstream magnetic field, indicated as B_{ISM} and B_{W} for the ISM and wind case, respectively².

The gray shaded area represents the range of typical values of the jet break time, $t_j \in [10^4, 10^6]$ s, as inferred from observations (Frail et al. 2001; Bloom et al. 2003; Ghirlanda et al. 2004; Racusin et al. 2009; Cenko et al. 2010). The change of behavior in each (solid) curve marks the transition between θ_c and θ_j . The dashed lines represent the results from Eq. 2, which are consistent with our calculations when $\theta_j > \theta_c$. For maximum photon energies larger than 3 keV, these curves represent the lower boundary of the 'permitted' parameter space.

3. X-ray data analysis and results

To obtain observational constraints on the maximum observed frequency from detected GRBs, we select six events observed by *Swift*/XRT at times $> 10^7$ s after their respective trigger of the *Swift*/BAT, and with measured redshifts. The selected bursts are: GRB 130427A, GRB 130702A, GRB 130925A, GRB 161219B, GRB 190829A and GRB 221009A. The redshifts and prompt emitted energies are reported in column 2 and 3 of Tab. 1. Their XRT lightcurves, which are taken directly from the *Swift*/XRT repository, are shown in Fig. A.1.

We downloaded their XRT spectral data at epochs $> 10^5$ s from the *Swift*/XRT repository³ (Evans et al. 2007, 2009, 2023). For each GRB, the time intervals where time-resolved spectra were extracted are reported in the third column of Tab. A.1, and highlighted in the corresponding light curves in Fig. A.1) by different colors.

Spectral analysis was performed with `Xspec v. 12.15.0`. We tested two models: an absorbed power-law model and an absorbed power-law with a high energy exponential cutoff. In both cases, we fixed the Galactic hydrogen-equivalent column density $N_{\text{H,Gal}}$ to the value corresponding to the GRB coordinates (Dickey & Lockman 1990; Kalberla et al. 2005; HI4PI Collaboration et al. 2016) as provided by the HEASARC service⁴ (see column 4 of Tab. 1). The intrinsic absorption N_{H} was left free to vary in the fits but as a common parameter for the spectra corresponding to different time bins of the same GRB.

We use the multiplicative model function `cflux` which returns the integrated de-absorbed fluxes $\log_{10} \text{Flux} (\text{erg cm}^{-2} \text{s}^{-1})$ within a given energy band ($E_{\text{min}} = 0.3$ keV and $E_{\text{max}} = 10$ keV in our case) for the given spectral model.

For the power-law model, the photon indices Γ_{XRT} ($dN/dE \propto E^{-\Gamma_{\text{XRT}}}$) are left free to vary in the different temporal bins of the same GRB. In the case where $h\nu_{\text{max}}$ moves into the XRT band, a softening of the spectral index is expected. The photon indices obtained by the power-law fits are shown in Fig. A.1 in the panels below the corresponding light curves, where the time intervals selected for the spectral analysis are highlighted in different colors. According to our data analysis, the photon indices at different time intervals of the same GRB are consistent

² Following Sagi & Nakar (2012), we consider B_{W} and n at $R = 10^{18}$ cm for the wind case.

³ <https://www.swift.ac.uk/index.php>

⁴ <https://heasarc.gsfc.nasa.gov/cgi-bin/Tools/w3nh/w3nh.pl>

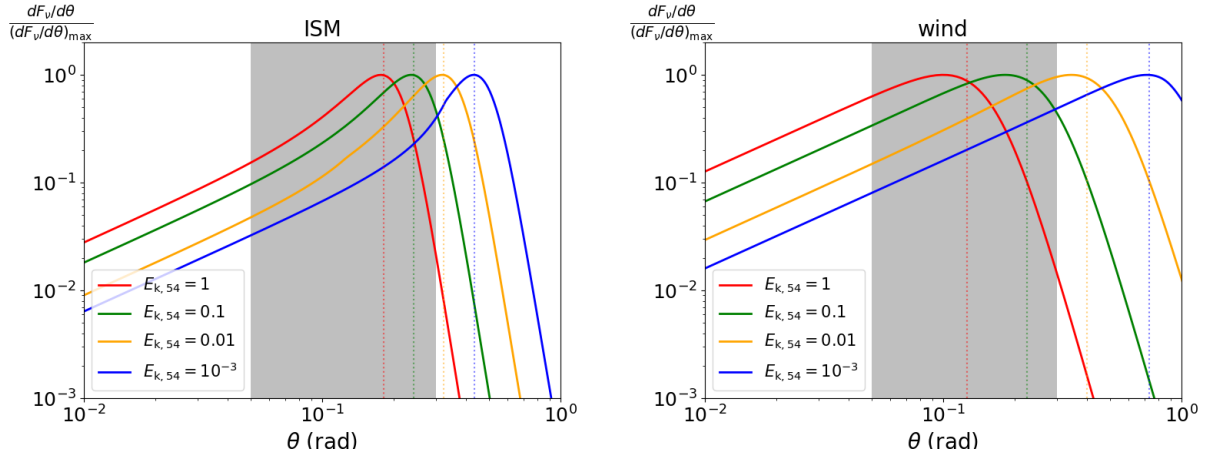


Fig. 2. Differential $dF_v/d\theta$ at $\nu/D > \nu'_c$ from different latitudes at the time $t = 3 \times 10^6$ s, adopting $p = 2.2$ and $z = 0.2$. The different line colors refer to different values of E_k . The dashed vertical lines indicate the values of θ_c and the gray shaded areas represent the typical range of values of the jet opening angle, $\theta_j \in [0.05, 0.3]$ radians. Left panel: ISM case with $n_0 = 0.1$. Right panel: wind case with $A_\star = 1$.

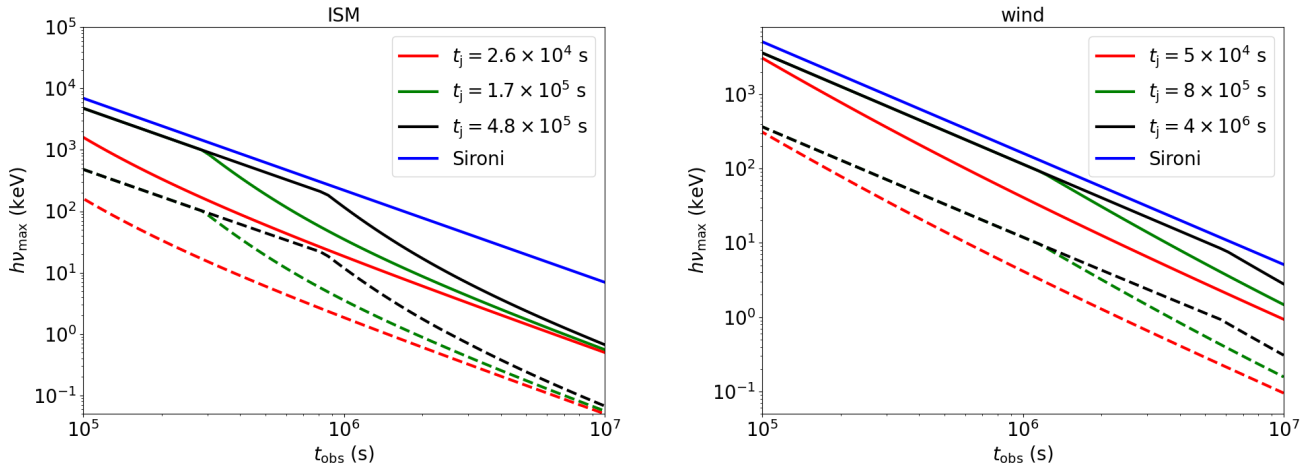


Fig. 3. Comparison between the predicted maximum synchrotron photon energy along the line of sight (blue curve, from Sironi et al. 2013) and that obtained when considering EATS and a conical geometry of the outflow. All curves are computed assuming $z = 0.2$, $\epsilon_{B,-3} = 15$ and $\sigma_{u,-9} = 3$. The black, green and red curves correspond to different jet break times t_j . Solid and dashed curves of the same color share the same t_j but differ in θ_j and $E_{k,54}/n_0$ (or $E_{k,54}/A_\star$ for the wind case). Left panel: ISM case with $n_0 = 1$. The solid curves correspond to $E_{k,54} = 1$ and $\theta_j = [0.05, 0.1, 0.15]$ rad, while the dashed curves correspond to $E_{k,54} = 0.01$ and $\theta_j = [0.09, 0.18, 0.27]$ rad. Right panel: wind case with $A_\star = 1$. The solid curves correspond to $E_{k,54} = 1$ and $\theta_j = [0.05, 0.1, 0.15]$ rad, while the dashed curves correspond to $E_{k,54} = 0.01$ and $\theta_j = [0.15, 0.32, 0.47]$ rad.

with each other within the error bars at 90% confidence ranges, and we find no clear evidence of a temporal softening, expected if a spectral break were to cross the XRT energy band from the higher to the lower energies.

In fitting this model, given the presence of an additional free parameter, we assumed (also supported by the results of the simple power-law model) that the photon index is time-independent across the spectra of the same burst (i.e. it is a free parameter common to all the time bins spectra of the same burst), while the cutoff energy is free to vary across different time bins. All fits are performed by exploring the free parameters with a Monte Carlo Markov Chain (MCMC), and their values are listed in Tab. A.1. The values of N_H in column 5 are adopted from the best fitting results using the power-law model. Only lower limits on the cutoff energy were found: their values (at 2σ confidence level) are listed in the last column of the Table.

4. Constraints from the absence of observed cutoffs

The lack of evidence for a spectral cut-off for the six GRBs examined imposes, for each of them, a lower limit on $h\nu_{\max}$ at the time t_{obs} when it was inferred. This in turn sets constraints on its physical parameters, as discussed in section 2.2 (see Fig. 4). Specifically, for each burst, we consider the time corresponding to the latest available XRT observation and the corresponding 2σ lower limits on the cutoff energy (as reported in Tab. A.1). These impose conservative constraints on the parameter space. As explained in the previous sections, these constraints depend on the jet break time we assume. The post-jet break light curve is expected to decay as $t^{-\alpha}$, with $3p/4 \leq \alpha \leq p$ (Gao et al. 2013; Rhoads 1999), depending on the external medium density profile (either uniform or wind-like) and on whether the forward shock undergoes significant lateral expansion. If the X-ray band

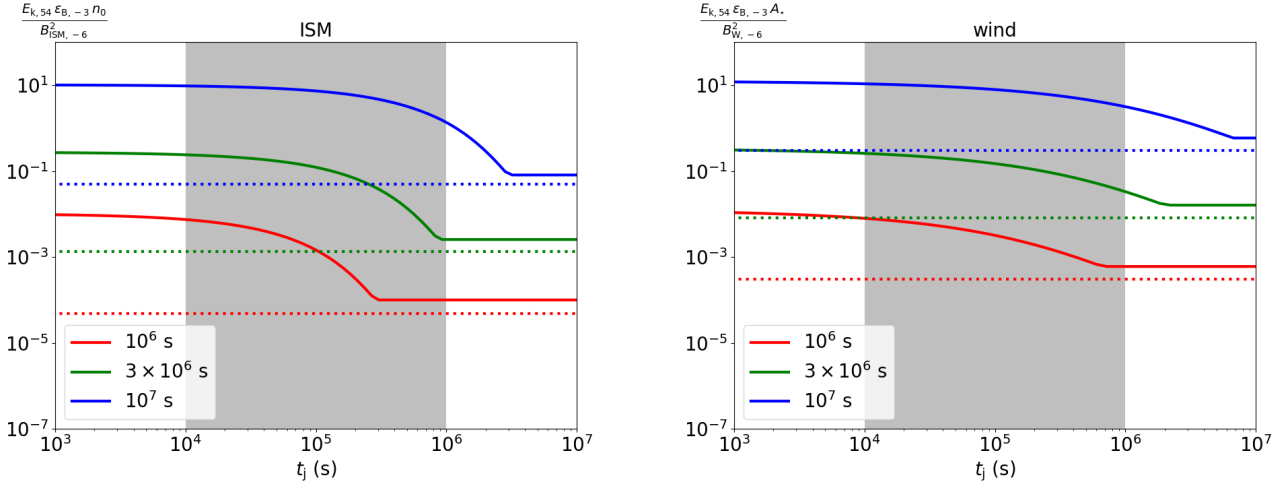


Fig. 4. Constraints on the parameter space for radiation with energy $h\nu_{\max} = 3$ keV observed at 10^6 , 3×10^6 and 10^7 s (for a source redshift $z = 0.2$). The gray shaded areas indicate the range of typical values of jet break times, $t_j \in [10^4, 10^6]$ s. Solid lines show the results in this work which accounts for the effect of EATS, while dotted lines reproduce the predictions of Sironi et al. (2013). Left panel: ISM case. Right panel: wind case.

is above ν_c , then the X-ray photon index Γ_{XRT} and the electron energy distribution index p are related by $p = 2\Gamma_{\text{XRT}} - 2$. With these notions in mind, a simple visual inspection of Figure A.1 shows that the late-time decay indices of the X-ray light curves of the examined GRB afterglows are all compatible with a post-jet-break phase, even though a pre-jet-break could still be accommodated if ν_c is instead above the X-ray band. In two cases (GRB 130925A and GRB 190829A) there is some evidence of a steepening at around 10^6 seconds, but it is not possible to conclusively determine whether this is related to a jet break without an in-depth analysis of the multi-wavelength dataset for each individual GRB. For these reasons, and for simplicity, we prefer to remain agnostic about the jet break time in the present analysis, showing our results as a function of t_j instead.

The results are reported in Fig. 5, which considers the same combination of parameters $[\epsilon_B, n_0(A_*)], B_{\text{ISM}}(B_W), E_k, t_j$ adopted in Fig. 4 and motivated in section 2.2. Note that in Fig. 5 we have replaced E_k with the radiative efficiency η_γ . For clarity of the figure, we define it as

$$\eta_\gamma = \frac{E_\gamma}{E_k}, \quad (18)$$

where E_γ is the isotropic equivalent gamma-ray energy detected during the prompt phase, that is known for the six GRBs under study (see Tab. 1). This definition differs from that more commonly used $\eta = \frac{E_\gamma}{E_\gamma + E_k}$ (Lloyd-Ronning & Zhang 2004; Zhang et al. 2007): clearly the two definitions are equivalent when $E_\gamma \ll E_k$. Estimates of the radiative efficiency have been reported in previous works (Zhang et al. 2007; Wang et al. 2015): its typical value is $\eta \sim 10\%$ (Du et al. 2016; Hascoët et al. 2014; Li et al. 2018; D'Avanzo et al. 2012), but it could be significantly larger in some GRBs (Lloyd-Ronning & Zhang 2004; Li & Wang 2024).

In Fig. 5 the six curves in different colors refer to the six GRBs. The gray shaded area indicates the range of typical values of the jet break time t_j and the values of the y-axis correspond to representative values of the relevant parameters. The vertical arrows indicate that the parameter space consistent with the observations, specifically the lower limit on the spectral cut-off energy for each GRB, is that above the corresponding curve.

Since only lower limits on the cutoff energy could be derived, the resulting constraints for all six GRBs are, at best, marginally consistent with typical afterglow parameters, unless their jet-break times are all rather late ($\gtrsim 10^6$ s).

The constraints are particularly tight, by 2-3 orders of magnitude in the combination of parameters given on the y-axis, for three GRBs, namely GRB 130702A, GRB 161219B and GRB 190829A (their curves are marked with particular patterns): to account for the lack of a spectral cut-off in their spectra, one should invoke a very low radiative efficiency, a very large ϵ_B , or a very high external density (or some combinations of these factors).

These GRBs have particularly low prompt energetics, smaller than 10^{51} erg (Golenetskii et al. 2013c; Frederiks et al. 2016; Lesage et al. 2019; Tsvetkova et al. 2019): since $h\nu_{\text{sat}} \propto E_k^{1/2}$, their late X-ray emission indeed provides the best opportunity to test for the presence of a cutoff or place the tighter constraints on the parameter space based on its absence. We note that the γ_{sat} model that we employ is based on PIC simulations of relativistic shocks with a Lorentz factor $\Gamma = 15$, and it is expected to be valid for shocks that are at least mildly relativistic. According to the analysis of Sironi et al. (2013), however, the particle acceleration in mildly relativistic shocks is less efficient due to a suppression of the Weibel and oblique instabilities, which are responsible for the generation of the magnetic turbulence that governs the Fermi process. The shock in the three weakest events is expected to decelerate to Lorentz factors $\Gamma_{\text{sh}} \lesssim 1.5$ unless the shock is particularly energetic or the external density sufficiently low. In the ISM case, this quantitatively translates into having $\eta_{\gamma,1} n_0 \lesssim 0.05 - 0.5$. For these three events, therefore, our results are conservative with respect to our conclusions.

5. Discussion and conclusions

We analyzed the X-ray synchrotron spectra of six GRBs during their late-time afterglow phase, searching for spectral cut-off signatures to probe the maximum energy achievable by electrons accelerated at relativistic shocks. The motivation is provided by the results of numerical simulations by Sironi et al. (2013), which predict the expected maximum energy of elec-

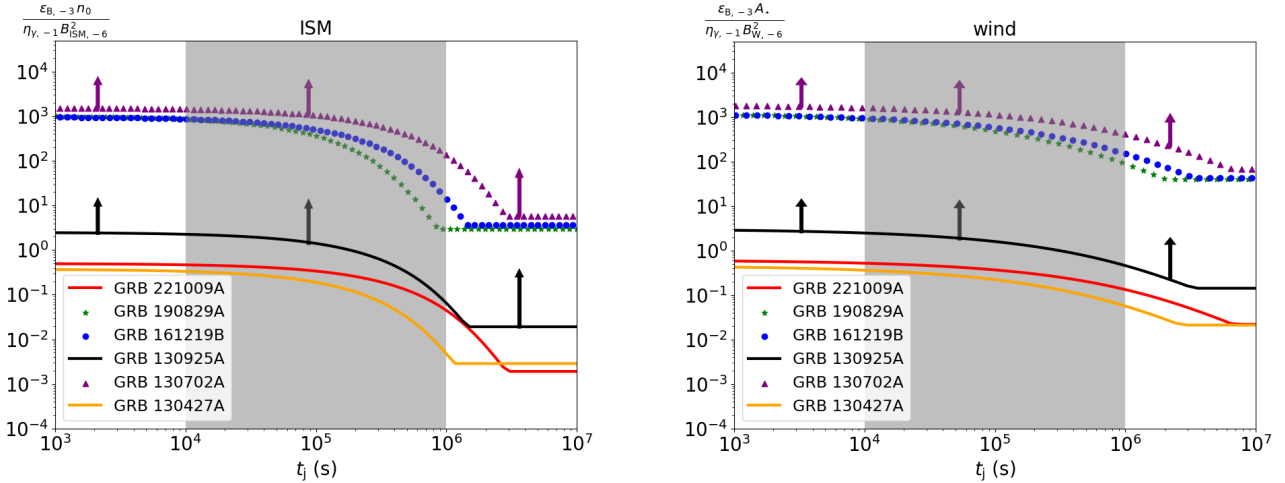


Fig. 5. Constraints on the parameter space derived from the spectral analysis of the six selected GRBs. Each curve is built considering the prompt emitted energy E_γ of the GRB (listed in Tab. 1) and the lower limit on $h\nu_{\max}$ obtained from our spectral analysis at a given observational time t_{obs} (see text for details). The gray shaded regions represent the typical range of the jet break time $t_j \in [10^4, 10^6]$ s and the values of the y-axis correspond to representative values of the relevant parameters. Arrows indicate that the curves represent lower bounds on the allowed parameter space. Left panel: ISM case. Right panel: wind case. The three GRBs with low E_γ - which, for standard values of the parameters, are in tensions with the predictions on $h\nu_{\max}$) - are marked with distinct symbols: \star for GRB 190829A, \bullet for GRB 161219B and \blacktriangle for GRB 130702A.

Table 1. GRBs analyzed in this work, listed together with their redshift z and energy E_γ emitted during the prompt phase.

Event	z	E_γ (erg)	References
GRB 221009A	0.151	3×10^{54}	1, 2
GRB 190829A	0.0785	2×10^{50}	3, 4
GRB 161219B	0.1475	1.6×10^{50}	5, 6
GRB 130925A	0.347	1.5×10^{53}	7, 8
GRB 130702A	0.145	6.4×10^{50}	9, 10
GRB 130427A	0.34	8.5×10^{53}	11, 12

References. (1) de Ugarte Postigo et al. (2022); (2) Frederiks et al. (2022); (3) Valeev et al. (2019); (4) Tsvetkova et al. (2019); (5) Tanvir et al. (2016); (6) Frederiks et al. (2016); (7) Vreeswijk et al. (2013); (8) Golenetskii et al. (2013b); (9) Leloudas et al. (2013); (10) Golenetskii et al. (2013c); (11) Levan et al. (2013); (12) Golenetskii et al. (2013a). For each GRB the first reference is for redshift, the second one for E_γ .

trons accelerated in relativistic, weakly magnetized shocks, and consequently the maximum achievable synchrotron photons energy.

We first showed that these predictions would imply a spectral cutoff that could enter the XRT energy band at late times ($10^6 - 10^7$ s). Before testing these predictions against observations, we refined the estimates on the maximum photon energy by accounting for EATS and the shock anisotropy induced by a jet's conical geometry. Our analysis focused on six GRB events with exceptionally late-time XRT detections. The data reveal no statistically significant evidence for a spectral cutoff within the XRT energy range. For each GRB, the 2σ lower limit on the cutoff energy provides constraints on the afterglow parameters under the assumption that the numerical results of Sironi et al. (2013) apply. We present our results for both an ISM and a wind environment. Although some (relatively small) quantitative differences are apparent between the two assumed environments, the overall conclusions of this work do not differ qualitatively between the two cases.

For typical values of the afterglow parameters, the non-detection of a spectral cutoff in the X-ray band for the three most energetic GRBs in our sample is at best marginally consistent with the theoretical predictions. The lower limit in the parameter space for these bursts (solid lines in Fig. 5) cluster around values of the order unity for the combination of parameters shown on the y-axis of the plot. This corresponds to typical afterglow parameters, namely a magnetic field fraction $\epsilon_B = 10^{-3}$, a circumburst density $\sim 1 \text{ cm}^{-3}$ (or $\sim A_*$), and prompt emission efficiency $\eta_\gamma = 10\%$, for jet break times $t_j \lesssim$ a few 10^5 s. We note that afterglow modeling (e.g., Beniamini et al. 2015; Wang et al. 2019; Salafia et al. 2022; Huang et al. 2022; Aharonian et al. 2023) commonly indicates values of ϵ_B in the range 10^{-5} to 10^{-3} , thus making the parameter space even more constrained.

For the three remaining GRBs (GRB 130702A, GRB 161219B and GRB 190829A), which are significantly less energetic, the constraints on the parameter space from the late-time spectral analysis (symbol lines in Fig. 5) could be satisfied only by invoking a very low radiative efficiency, $\eta_\gamma < 1\%$, or very large $\epsilon_B \sim 1$ or densities ($n \sim 10^3 \text{ cm}^{-3}$). Small values of the prompt efficiency would imply an extremely large requirement on the total energetics and both such large ϵ_B and densities are at odds with results from afterglow modeling.

In light of these results, it is difficult to reconcile the maximum synchrotron photon energy predicted by numerical simulations with the observations, thus putting into question our understanding of particle acceleration mechanisms. Possible factors that could alleviate — or even resolve — this tension, by allowing for higher maximum energies of electrons accelerated at relativistic shocks, are worth mentioning.

The saturation limit of the accelerated electron energy is proportional to the characteristic length scale of turbulence triggered by the Weibel instability, such that $\gamma_{\text{sat}} \propto \lambda_w$ (Reville & Bell 2014; Huang et al. 2022). This length scale can be expressed as $\lambda_w = \ell_w c / \omega_p$ (Sironi et al. 2013; Reville & Bell 2014), where ω_p is the relativistic plasma frequency. Hence the maximum synchrotron photon energy scales as $h\nu_{\text{sat}} \propto \ell_w^2$. Values of $\ell_w \sim 10$ were inferred from the numerical simulations by Sironi

& Spitkovsky (2009a) and Sironi et al. (2013) and adopted in the estimates of $h\nu_{\text{sat}}$ throughout this work. However recent PIC simulations of unprecedented size and duration by Grošelj et al. (2024) indicate that the turbulence scale can approach $100 c/\omega_p$ and may continue to grow beyond the simulated time span. The expected $h\nu_{\text{sat}}$ can therefore be enhanced by at least two orders of magnitude and relax the constraints on the parameter space.

Other physical mechanisms could also increase the maximum electron energy beyond saturation limit predicted by Sironi et al. (2013). Using both analytical and numerical approaches, Huang et al. (2023) and Kirk et al. (2023) found that efficient particle acceleration at relativistic shocks can persist after particles reach the downstream saturation limit, as long as their upstream trajectories are dominated by random scattering rather than by gyro-motion. Furthermore, the three-dimensional structure of pre-existing magnetic fields may also come into play (Giacinti & Kirk 2018; Huang et al. 2023). For example, in a toroidal magnetic-field configuration, particles with the favorable charge experience a curvature drift along the shock velocity, which can increase both the acceleration efficiency and the maximum achievable energy (Huang et al. 2023).

In this paper, we focus on XRT afterglow detections at very late times ($> 10^6$ s), under the assumption that the predictions of Sironi et al. (2013), which are gauged for highly relativistic shocks, are still valid. According to their analysis, our conclusions should be even stronger for mildly relativistic shocks, which could be the case for the three weakest events in our sample.

Clearly, the selection of the six events is influenced by observational constraints and limitations. It is not obvious how such biases affect our findings: however the requirement of detectable flux at late times might lead to a preferential selection of GRBs with particularly late jet break times and thus, as shown, relax the constraints somewhat.

To mitigate these limitations and ease the requirement for very late-time observations, further tests of our results and tighter constraints on particle-acceleration models in this context, could be achieved by analyzing afterglow spectra at higher photon energies, above 10 keV, as a spectral cutoff is expected to enter higher-energy bands at earlier times. A less extreme requirement on the detection time might also enlarge the sample of GRBs which can provide relevant constraints. For instance, NuSTAR can detect photons up to ~ 80 keV, enabling our conclusions to be tested with observations at $\sim 10^6$ s. Detections at even earlier epochs, around $\sim 10^5$ s, could become feasible with future MeV-band experiments.

Acknowledgements. This study was funded by the European Union - NextGenerationEU, in the framework of the PRIN Project "PEACE: Powerful Emission and Acceleration in the most powerful Cosmic Explosion" (code 202298J7KT-CUP G53D23000880006). The views and opinions expressed are solely those of the authors and do not necessarily reflect those of the European Union, nor can the European Union be held responsible for them. We acknowledge financial support from an INAF Mini Grant 2022 (PI L. Nava). This work made use of data supplied by the UK Swift Science Data Centre at the University of Leicester.

References

Ackermann, M., Ajello, M., Asano, K., et al. 2014, Science, 343, 42

Aharonian, F., Ait Benkhali, F., Aschersleben, J., et al. 2023, ApJ, 946, L27

Beniamini, P., Nava, L., Duran, R. B., & Piran, T. 2015, MNRAS, 454, 1073

Blandford, R. D. & McKee, C. F. 1976, Physics of Fluids, 19, 1130

Bloom, J. S., Frail, D. A., & Kulkarni, S. R. 2003, ApJ, 594, 674

Cenko, S. B., Frail, D. A., Harrison, F. A., et al. 2010, ApJ, 711, 641

Chevalier, R. A. & Li, Z.-Y. 2000, ApJ, 536, 195

Chiang, J. & Dermer, C. D. 1999, ApJ, 512, 699

D'Avanzo, P., Salvaterra, R., Sbarufatti, B., et al. 2012, MNRAS, 425, 506

de Jager, O. C., Harding, A. K., Michelson, P. F., et al. 1996, ApJ, 457, 253

de Ugarte Postigo, A., Izzo, L., Pugliese, G., et al. 2022, GRB Coordinates Network, 32648, 1

Dermer, C. D. & Chiang, J. 1998, New A, 3, 157

Dermer, C. D. & Menon, G. 2009, High Energy Radiation from Black Holes: Gamma Rays, Cosmic Rays, and Neutrinos (Princeton University Press)

Dickey, J. M. & Lockman, F. J. 1990, ARA&A, 28, 215

Du, S., Lü, H.-J., Zhong, S.-Q., & Liang, E.-W. 2016, MNRAS, 462, 2990

Evans, P. A., Beardmore, A. P., Page, K. L., et al. 2009, MNRAS, 397, 1177

Evans, P. A., Beardmore, A. P., Page, K. L., et al. 2007, A&A, 469, 379

Evans, P. A., Page, K. L., Beardmore, A. P., et al. 2023, MNRAS, 518, 174

Fong, W., Berger, E., Margutti, R., et al. 2012, ApJ, 756, 189

Frail, D. A., Kulkarni, S. R., Sari, R., et al. 2001, ApJ, 562, L55

Frederiks, D., Golenetskii, S., Aptekar, R., et al. 2016, GRB Coordinates Network, 20323, 1

Frederiks, D., Lysenko, A., Ridnaia, A., et al. 2022, GRB Coordinates Network, 32668, 1

Gao, H., Lei, W.-H., Zou, Y.-C., Wu, X.-F., & Zhang, B. 2013, New A Rev., 57, 141

Ghirlanda, G., Ghisellini, G., & Lazzati, D. 2004, ApJ, 616, 331

Giacinti, G. & Kirk, J. G. 2018, ApJ, 863, 18

Golenetskii, S., Aptekar, R., Frederiks, D., et al. 2013a, GRB Coordinates Network, 14487, 1

Golenetskii, S., Aptekar, R., Frederiks, D., et al. 2013b, GRB Coordinates Network, 15260, 1

Golenetskii, S., Aptekar, R., Pal'Shin, V., et al. 2013c, GRB Coordinates Network, 14986, 1

Granot, J. & Sari, R. 2002, ApJ, 568, 820

Grošelj, D., Sironi, L., & Spitkovsky, A. 2024, ApJ, 963, L44

Hascoët, R., Daigne, F., & Mochkovitch, R. 2014, MNRAS, 442, 20

HI4PI Collaboration, Ben Bekhti, N., Flöer, L., et al. 2016, A&A, 594, A116

Huang, Y.-F., Lu, Y., Wong, A. Y. L., & Cheng, K. S. 2007, Chinese J. Astron. Astrophys., 7, 397

Huang, Z.-Q., Kirk, J. G., Giacinti, G., & Reville, B. 2022, ApJ, 925, 182

Huang, Z.-Q., Reville, B., Kirk, J. G., & Giacinti, G. 2023, MNRAS, 522, 4955

Kalberla, P. M. W., Burton, W. B., Hartmann, D., et al. 2005, A&A, 440, 775

Kirk, J. G., Reville, B., & Huang, Z.-Q. 2023, MNRAS, 519, 1022

Leloudas, G., Fynbo, J. P. U., Schulze, S., et al. 2013, GRB Coordinates Network, 14983, 1

Lesage, S., Poolakkil, S., Fletcher, C., et al. 2019, GRB Coordinates Network, 25575, 1

Levan, A. J., Cenko, S. B., Perley, D. A., & Tanvir, N. R. 2013, GRB Coordinates Network, 14455, 1

Li, L. & Wang, Y. 2024, ApJ, 972, 195

Li, L., Wu, X.-F., Lei, W.-H., et al. 2018, ApJS, 236, 26

Lloyd-Ronning, N. M. & Zhang, B. 2004, ApJ, 613, 477

Medvedev, M. V. & Loeb, A. 1999, ApJ, 526, 697

Meszaros, P., Rees, M. J., & Papathanassiou, H. 1994, ApJ, 432, 181

Panaiteescu, A. & Mészáros, P. 1998, ApJ, 493, L31

Pennanen, T., Vurm, I., & Poutanen, J. 2014, A&A, 564, A77

Piran, T. & Nakar, E. 2010, ApJ, 718, L63

Racusin, J. L., Liang, E. W., Burrows, D. N., et al. 2009, ApJ, 698, 43

Reville, B. & Bell, A. R. 2014, MNRAS, 439, 2050

Rhoads, J. E. 1999, ApJ, 525, 737

Sagi, E. & Nakar, E. 2012, ApJ, 749, 80

Salafia, O. S., Ravasio, M. E., Yang, J., et al. 2022, ApJ, 931, L19

Sari, R. 1997, ApJ, 489, L37

Sari, R. 1998, ApJ, 494, L49

Sari, R. & Esin, A. A. 2001, ApJ, 548, 787

Sari, R., Piran, T., & Narayan, R. 1998, ApJ, 497, L17

Sironi, L. & Spitkovsky, A. 2009a, ApJ, 698, 1523

Sironi, L. & Spitkovsky, A. 2009b, ApJ, 707, L92

Sironi, L., Spitkovsky, A., & Arons, J. 2013, ApJ, 771, 54

Spitkovsky, A. 2005, in American Institute of Physics Conference Series, Vol. 801, Astrophysical Sources of High Energy Particles and Radiation, ed. T. Bulik, B. Rudak, & G. Madejski (AIP), 345–350

Spitkovsky, A. 2008, ApJ, 673, L39

Tanvir, N. R., Kruehler, T., Wiersema, K., et al. 2016, GRB Coordinates Network, 20321, 1

Tsvetkova, A., Golenetskii, S., Aptekar, R., et al. 2019, GRB Coordinates Network, 25660, 1

Valeev, A. F., Castro-Tirado, A. J., Hu, Y. D., et al. 2019, GRB Coordinates Network, 25565, 1

Vreeswijk, P. M., Malesani, D., Fynbo, J. P. U., De Cia, A., & Ledoux, C. 2013, GRB Coordinates Network, 15249, 1

Wang, X.-G., Zhang, B., Liang, E.-W., et al. 2015, ApJS, 219, 9

Wang, X.-Y., Liu, R.-Y., Zhang, H.-M., Xi, S.-Q., & Zhang, B. 2019, ApJ, 884, 117

Weibel, E. S. 1959, Phys. Rev. Lett., 2, 83

Zhang, B., Liang, E., Page, K. L., et al. 2007, ApJ, 655, 989

Appendix A: Fitting results

The fitting parameters obtained from the MCMC analysis assuming a cutoff power-law model are listed in Tab. A.1.

Figure A.1 shows the unabsorbed XRT light curves in the 0.3–10 keV energy band for the six GRBs at times $\gtrsim 10^5$ s. Different colors indicate the time intervals selected for the spectral analysis. The lower panels display the corresponding time evolution of the photon indices Γ_{XRT} derived from single power-law fits. If $h\nu_{\text{max}}$ enters the X-ray band, a spectral cutoff is expected, leading to a softening of the X-ray spectra. However, our analysis shows that, for each GRB, the photon indices measured at different time intervals are mutually consistent within the uncertainties.

Appendix B: Derivation of the dependency of the $h\nu_{\text{max}}$ evolution on the jet break time t_j

In this Appendix we explicitly show that the evolution of the maximum synchrotron frequency normalized to its value at the jet break, that is $h\nu_{\text{max}}(t_{\text{obs}})/h\nu_{\text{max}}(t_j)$, depends only on t_{obs}/t_j . To see this, let us first demonstrate that, when $t_{\text{obs}} > t_j$, $h\nu_{\text{max}}(t_{\text{obs}})/h\nu_{\text{max}}(t_j)$ depends only on $\Gamma \theta_j$. In general, at a given latitude in the EATS, we can write

$$h\nu_{\text{max}}(t_{\text{obs}}, \theta) = \mathcal{D}(t_{\text{obs}}, \theta) \gamma_{\text{max}}^2(R(t_{\text{obs}}, \theta)) \frac{h e B(R(t_{\text{obs}}, \theta))}{2\pi m_e c}. \quad (\text{B.1})$$

It is straightforward to show that $\gamma_{\text{max}}(R) \propto \Gamma(R)$ and that the magnetic field scales as $B(R) \propto \Gamma(R)$. Moreover, by using the small-angle approximation for $\cos \theta$ and the second-order expansion of β in terms of Γ in the definition of the Doppler factor, one finds $\mathcal{D} \sim 2\Gamma/(1+(\Gamma\theta)^2)$. For $t_{\text{obs}} > t_j$, the latitude that dominates the observed emission is $\theta = \theta_j$, hence

$$\frac{h\nu_{\text{max}}(t_{\text{obs}})}{h\nu_{\text{max}}(t_j)} = \left(\frac{\Gamma(t_{\text{obs}}, \theta_j)}{\Gamma(t_j, \theta_j)} \right)^4 \frac{1 + \Gamma^2(t_j, \theta_j) \theta_j^2}{1 + \Gamma^2(t_{\text{obs}}, \theta_j) \theta_j^2}. \quad (\text{B.2})$$

Because $\Gamma(t_j, \theta_j) = \theta_j^{-1}$, the above expression becomes

$$\frac{h\nu_{\text{max}}(t_{\text{obs}})}{h\nu_{\text{max}}(t_j)} = 2 \frac{\left(\Gamma(t_{\text{obs}}, \theta_j) \theta_j \right)^4}{1 + \Gamma^2(t_{\text{obs}}, \theta_j) \theta_j^2}, \quad (\text{B.3})$$

which is a function of $\Gamma \theta_j$ only.

We now demonstrate that, in turn, $\Gamma \theta_j$ depends only on t_{obs}/t_j . First, we combine Eqs. 3 and 6 to write a proportionality relation between Γ_{sh} , θ and t_{obs} on the EATS, that is

$$t_{\text{obs}} \propto \left[\frac{E_k}{A} \right]^{1/(3-k)} \Gamma_{\text{sh}}^{-2/(3-k)}(\theta) \left[1 - \cos \theta + \frac{1}{2(4-k) \Gamma_{\text{sh}}^2(\theta)} \right]. \quad (\text{B.4})$$

Let us take the above relation evaluated at θ_j , divide both sides by $t_j \propto (E_k/A)^{1/(3-k)} \theta_j^{2(4-k)/(3-k)}$, and use the small-angle approximation $\cos \theta_j \approx 1 - \theta_j^2/2$. After some algebraic manipulation, we obtain

$$\frac{t_{\text{obs}}}{t_j} \propto \left(\Gamma_{\text{sh}} \theta_j \right)^{-2(4-k)/(3-k)} \left[1 + \left(\Gamma_{\text{sh}} \theta_j \right)^2 \right] \equiv \mathcal{F}(\Gamma \theta_j), \quad (\text{B.5})$$

where we used the fact that $\Gamma_{\text{sh}} \sim \sqrt{2}\Gamma$ to express the right-hand side in terms of the quantity $\Gamma \theta_j$. Since the function $\mathcal{F}(x)$ is monotonic, it can be inverted, so that $\Gamma \theta_j \propto \mathcal{F}^{-1}(t_{\text{obs}}/t_j)$. This result demonstrates that the ratio $h\nu_{\text{max}}(t_{\text{obs}})/h\nu_{\text{max}}(t_j)$ depends only on the ratio t_{obs}/t_j .

Table A.1. Parameters used to fit the six selected GRBs with the cutoff power-law model. To construct Fig. 5, we adopt, for each GRB, the start time of the latest time interval and the corresponding 2σ lower limit on E_{cut} , thus deriving the most conservative constraints on the parameter space.

GRB	z	t^a (s)	$N_{\text{H,Gal}}^b$ ($\times 10^{22} \text{ cm}^{-2}$)	N_{H}^c ($\times 10^{22} \text{ cm}^{-2}$)	$\log_{10}\text{Flux}^d$ (cgs)	Γ_{XRT}^e	$\log_{10}(E_{\text{cut}}/\text{keV})^f$
221009A	0.151	$7 \times 10^5 - 10^6$	0.443	0.604	$-10.88^{+0.02}_{-0.02}$	$1.84^{+0.07}_{-0.11}$	>1.10
		$10^6 - 3 \times 10^6$			$-11.40^{+0.02}_{-0.02}$		>1.24
		$3 \times 10^6 - 7 \times 10^6$			$-11.90^{+0.03}_{-0.03}$		>0.98
		$10^7 - 2 \times 10^7$			$-13.02^{+0.10}_{-0.11}$		>0.68
190829A	0.0785	$3 \times 10^5 - 7 \times 10^5$	0.0466	0.749	$-11.36^{+0.04}_{-0.05}$	$2.29^{+0.15}_{-0.21}$	>0.95
		$7 \times 10^5 - 3 \times 10^6$			$-11.94^{+0.05}_{-0.05}$		>0.77
		$3 \times 10^6 - 10^7$			$-12.76^{+0.10}_{-0.10}$		>1.03
161219B	0.1475	$10^5 - 5 \times 10^5$	0.0294	0.172	$-11.33^{+0.03}_{-0.03}$	$1.76^{+0.10}_{-0.11}$	>0.83
		$5 \times 10^5 - 10^6$			$-11.71^{+0.04}_{-0.03}$		>1.34
		$10^6 - 5 \times 10^6$			$-12.24^{+0.04}_{-0.04}$		>0.89
		$5 \times 10^6 - 2 \times 10^7$			$-12.93^{+0.08}_{-0.09}$		>0.64
130925A	0.347	$2 \times 10^5 - 5 \times 10^5$	0.016	1.962	$-10.41^{+0.06}_{-0.06}$	$3.72^{+0.11}_{-0.18}$	>0.89
		$5 \times 10^5 - 2 \times 10^6$			$-11.08^{+0.06}_{-0.06}$		>0.76
		$2 \times 10^6 - 5 \times 10^6$			$-11.72^{+0.09}_{-0.10}$		>0.72
		$5 \times 10^6 - 2 \times 10^7$			$-12.43^{+0.13}_{-0.14}$		>0.83
130702A	0.145	$1 \times 10^5 - 6 \times 10^5$	0.0149	0.085	$-11.38^{+0.03}_{-0.03}$	$1.73^{+0.08}_{-0.10}$	>0.95
		$6 \times 10^5 - 2 \times 10^6$			$-12.03^{+0.03}_{-0.03}$		>1.06
		$2 \times 10^6 - 7 \times 10^6$			$-12.77^{+0.04}_{-0.05}$		>1.09
		$10^7 - 2 \times 10^7$			$-13.53^{+0.12}_{-0.14}$		>0.59
130427A	0.34	$1 \times 10^5 - 7 \times 10^5$	0.0164	0.073	$-11.07^{+0.01}_{-0.01}$	$1.63^{+0.04}_{-0.05}$	>1.38
		$7 \times 10^5 - 4 \times 10^6$			$-12.04^{+0.02}_{-0.02}$		>1.25
		$4 \times 10^6 - 2 \times 10^7$			$-12.99^{+0.05}_{-0.06}$		>0.94

Notes. ^a Time intervals in which we analyze the spectral data. ^b Galactic hydrogen equivalent column density. ^c Intrinsic hydrogen equivalent column density (at the source redshift). ^d Integrated flux in 0.3 - 10 keV energy band. ^e Photon spectral index. ^f Lower limit on E_{cut} at 2σ confidence level.

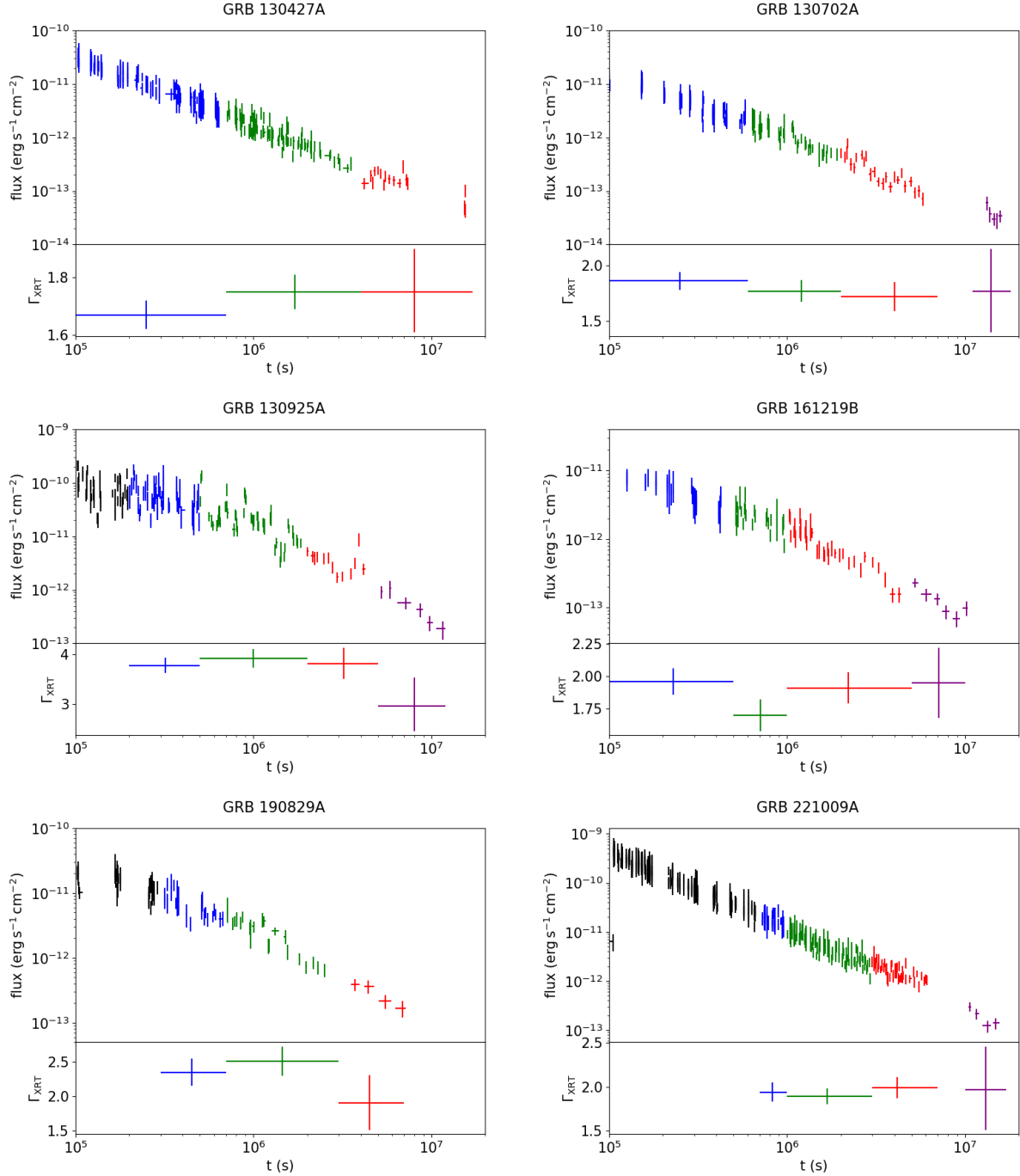


Fig. A.1. The top panels show the late-time ($\gtrsim 10^5$ s) unabsorbed X-ray (0.3–10 keV) light curves of the six GRBs analyzed in this work, obtained from the *Swift*/XRT repository. Different colors indicate the time intervals selected for the spectral analysis. The bottom panels display the corresponding photon indices derived from single power-law spectral fits and listed in Tab. A.1).